

Compact Binary Systems Waveform Generation with Generative Pre-trained Transformer

Ruijun Shi,^{1,*} Yue Zhou,^{2,*} Tianyu Zhao,^{1,2} Zhoujian Cao,¹ and Zhixiang Ren^{2,†}

¹*Department of Astronomy, Beijing Normal University, Beijing 100875, China*

²*Peng Cheng Laboratory, Shenzhen 518055, China*

(Dated: September 26, 2024)

Space-based gravitational wave detection is one of the most anticipated gravitational wave (GW) detection projects in the next decade, which will detect abundant compact binary systems. However, the precise prediction of space GW waveforms remains unexplored. To solve the data processing difficulty in the increasing waveform complexity caused by detectors' response and second-generation time-delay interferometry (TDI 2.0), an interpretable pre-trained large model named **CBS-GPT** (Compact Binary Systems Waveform Generation with Generative Pre-trained Transformer) is proposed. For compact binary system waveforms, three models were trained to predict the waveforms of massive black hole binary (MBHB), extreme mass-ratio inspirals (EMRIs), and galactic binary (GB), achieving prediction accuracies of 98%, 91%, and 99%, respectively. The CBS-GPT model exhibits notable interpretability, with its hidden parameters effectively capturing the intricate information of waveforms, even with complex instrument response and a wide parameter range. Our research demonstrates the potential of large pre-trained models in gravitational wave data processing, opening up new opportunities for future tasks such as gap completion, GW signal detection, and signal noise reduction.

I. INTRODUCTION

The first direct detection of binary black hole merger event (GW150914)[1, 2] by Laser Interferometer Gravitational-Wave Observatory (LIGO) has opened an innovative window to understand the universe, which provides direct evidence for the validity of Einstein's General Relativity. Gravitational wave (GW) observations will clarify many questions in astrophysics, cosmology, and fundamental physics[3–10]. So far, the ground-based gravitational wave detector has reported over a hundred compact binary coalesces (CBC) events[11], and recently pulsar timing array (PTA) has also successfully detected sound evidence of the existence of Stochastic Gravitational Wave Background (SGWB)[12–15]. To gain a deeper understanding and an overall picture of gravitational wave cosmology[16], the field of low-frequency gravitational waves needs to be widely covered. Hence, space-based gravitational wave detector projects have been launched. For example, Laser Interferometer Space Antenna (LISA)[17], Taiji[18, 19] and Tianqin[20] are all scheduled for the 2030s. The space-based gravitational wave detection could avoid terrestrial noise[21] and make the detection of low-frequency (10^{-4} –0.1Hz) gravitational wave signals more promising. In particular, future space-based gravitational wave detections are expected to detect a richer variety of gravitational wave sources including massive black hole binary (MBHB), extreme mass-ratio inspirals (EMRIs), and galactic binary (GB)[17].

In space-based and ground-based detections, GW signals are both extremely weak and usually buried in instrumental noise. Traditional methods will face challenges in

meeting the demands of gravitational wave data analysis in the future. Artificial Intelligence (AI)-driven frameworks have shed some new light on this issue. Specifically, AI techniques have been successfully applied in various subjects such as gravitational wave signal detection[22–27], parameter estimation[28–30], signal extraction[31] and noise reduction[32–35] with promising results. Additionally, the target of space gravitational wave detectors is also one type of complex and multi-scale waveforms (such as MBHB, EMRIs, and GB). Therefore, AI is expected to be a valuable tool for understanding and predicting waveform, as well as providing guidance and enlightenment on data-driven methods for GW framework design in the near future. Some previous studies focused on generating black hole binaries (BHB) waveforms. Lee et al.[36] employed a Recurrent Neural Network (RNN) that is capable of generating BHB waveforms during the merging and ring-down phases of non-spinning binary black hole coalescence. Khan et al.[37] demonstrated that vanilla transformer can learn quasi-circular, spinning, non-precessing binary black hole mergers waveform. Similarly, Chua et al.[38] used a greedy algorithm to build a reduced basis, allowing for the rapid generation of BHB waveforms. Recently, large-scale language models (LLM) based on attention mechanism have shown their tremendous power[39–42]. Some studies indicate that similar architectures can be applied to the GW data analysis[31, 35]. Developing a deep learning data processing framework for space-based GW detection is an impending necessity.

However, the above investigations did not consider the space-based GW detectors' response, and the second-generation time-delay interferometry (TDI 2.0) combinations. Moreover, prior investigations have limited their analysis to a restricted range of waveform parameters. In our paper, we are dedicated to further investigation on more complex waveforms and training a pre-trained model

* Equal contribution

† Corresponding author; renzhx@pcl.ac.cn

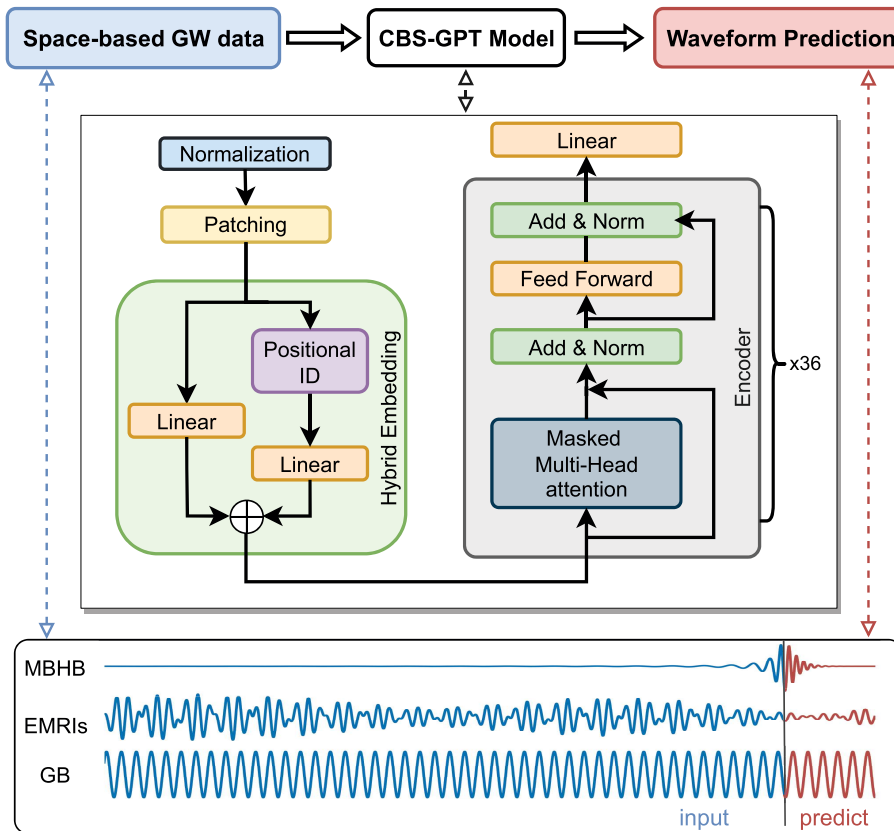


Figure 1. **Overview of CBS-GPT pipeline.** Inputs contain three kinds of GW sources (MBHB, EMRIs, and gb), after feeding into CBS-GPT, the successive waveforms are extrapolated.

to facilitate solving downstream problems. Hence, we proposed **CBS-GPT** (Compact **B**inary **S**ystems **W**aveform **G**eneration with **G**enerative **P**re-trained **T**ransformer) model, which is an interpretable, transformer-based, and self-supervised large model for prediction of compact binary sources (MBHB, EMRIs, and GB). In CBS-GPT, patching and hybrid embedding mechanisms are proposed for full extraction of waveform features. By utilizing the self-attention mechanism and mean square error loss, CBS-GPT is trained for each GW waveform source. The experiment results illustrate that CBS-GPT can accurately predict the subsequent waveform based on the input waveform. The average overlap between the predicted and target waveforms of MBHB, EMRIs, and GB reaches 0.981, 0.912, and 0.991, respectively. We have also discovered that waveform complexity can significantly influence the model’s prediction performance and CBS-GPT can match the key frequencies effectively. Finally, through attention map visualization and calculating the correlation between the waveform and hidden parameters of the model, we discover that CBS-GPT can pay attention to the area with the same phase, confirming that CBS-GPT can adapt itself to learn waveform features even under complex instrument response and wide parameter range.

The rest of this paper is organized as follows. Section II

describes data generation and the CBS-GPT model architecture. In Section III, we present our overlap and attention map results and discuss the overlap and CBS-GPT interpretability outcomes. Finally, Section IV highlights our findings and proposes potential future research based on the results.

II. METHODOLOGY

A. Data

Space-based GW detectors’ targets are GW signals at frequencies of $[10^{-4}, 0.1]$ Hz. We focus on three compact binary sources that are of major interest to LISA: MBHB, EMRIs, and GB. Figure 2 displays data examples. Detailed information of the data generation process is given below.

1. MBHB

MBHB is one of LISA’s main detection targets[17]. The mass spectrum, formation, and evolution of MBHB, as

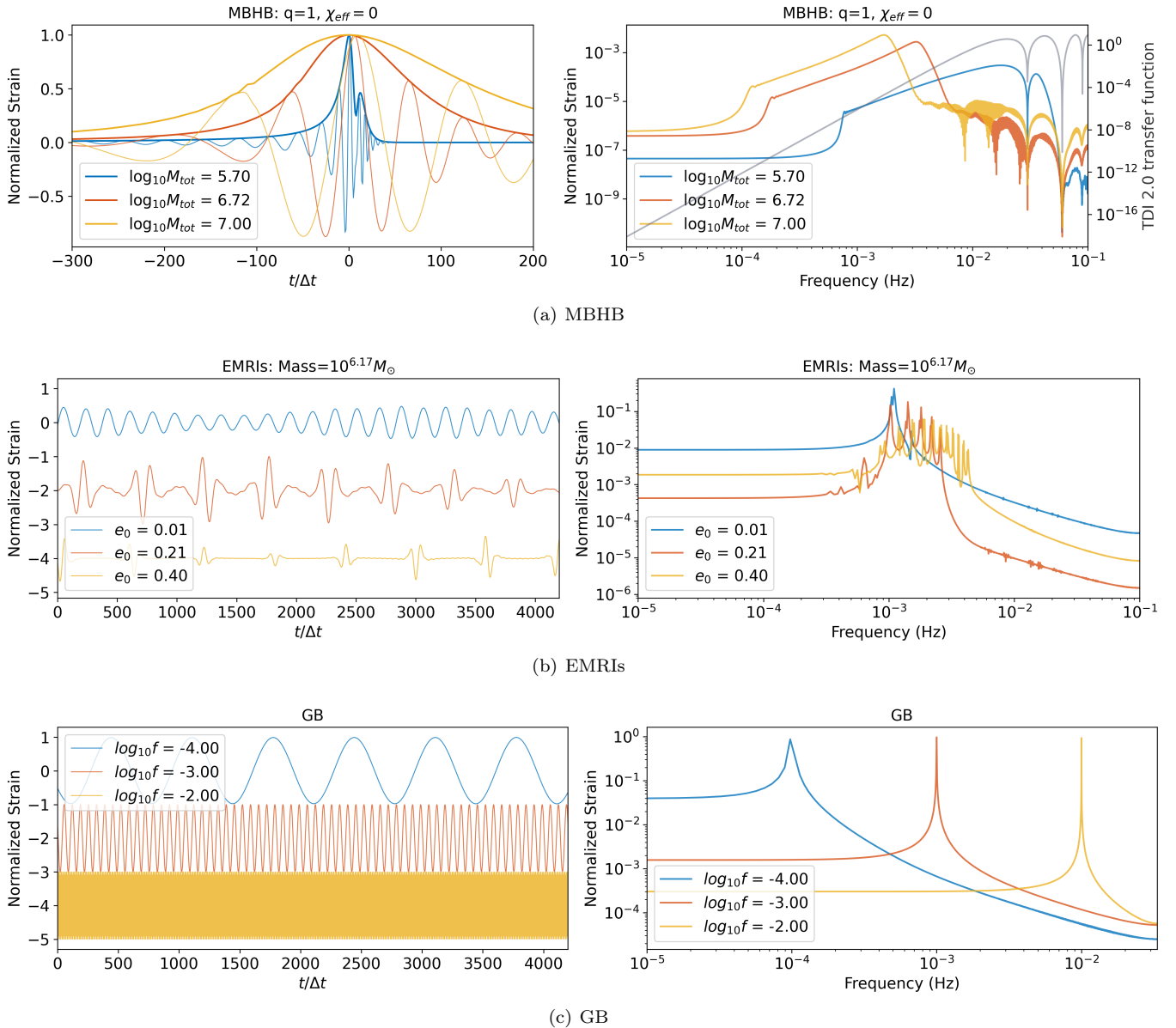


Figure 2. **TDI2.0 response complicates waveforms.** To simplify waveform comparison here, all waveforms were normalized to have a maximum amplitude of 1. The Δt in the figure represents the sampling rate. The effects of different parameters on time and frequency domain are shown on the left and right panels, respectively. (a) **MBHB waveforms** at different M_{tot} . At high frequencies, the TDI response function has a greater impact. The gray line represents the TDI 2.0 transfer function in the frequency domain. (b) **EMRIs waveforms** at different e_0 . As the eccentricity increases, the EMRIs waveform becomes more and more complex in the frequency domain. (c) **GB waveforms** at different f . The GB signal is relatively simple and is a single-frequency signal.

well as the interplay between MBHB and their host galaxies, can all be better understood through observations. In this paper, SEOBNRv4_opt[43] with including $l = m = 2$ mode is used to generate MBHB waveform. The parameter space of the MBHB dataset is shown in Table I(a). In Figure 2(a), the TDI 2.0 transfer function significantly affects high-frequency transmissions due to the lower total mass of MBHB. Firstly, we generate MBHB time-series waveforms with a length of 20,000 points with a sampling

rate of 5 seconds. During the training phase, each sample of training waveforms is truncated to 4,200 points, with 4,000 before and 200 points after the location of merge time. During the inference phase, the 4,000 valid points before the merge time are fed into CBS-GPT to predict the succeeding 200 points, hence achieving a 20:1 extrapolation prediction of MBHB waveform.

Table I. Parameters distribution of training set and test set

(a) Parameters space of MBHB dataset		
Parameter	Description	Parameter distribution
M_{tot}	Total mass of massive black hole binaries $m_1 + m_2$	log-Uniform $[5.5, 7]M_\odot$
q	Mass ratio $\frac{m_2}{m_1}$	Uniform $[0.1, 1]$
S_1^z, S_2^z	Spin parameters of two black holes	Uniform $[-0.99, 0.99]$
ι, ψ	The inclination angle and polarization angle	Uniform $[0, \pi]$
ϕ_c	Coalescence phase.	Uniform $[0, 2\pi]$
λ	Ecliptic longitude	Uniform $[0, 2\pi]$
β	Ecliptic latitude	Uniform $[0, \pi]$

(b) Parameters space of EMRIs dataset		
Parameter	Description	Parameter distribution
M	The mass of massive black hole (MBH)	Uniform $[10^5 - 10^7]M_\odot$
m	The mass of stellar-mass compact	Fix $[10M_\odot]$
a	Spin parameter of MBH	Uniform $[10^{-3}, 0.8]$
p_0	Semi-latus rectum	Uniform $[10, 16]$
e_0	Eccentricity	Uniform $[10^{-3}, 0.4]$
ι_0	The orbit's inclination angle from the equatorial plane	Uniform $[-0.98, 0.98]$
θ_S, ϕ_S	The polar and azimuthal sky location angle	Uniform $[10^{-3}, \pi]$
θ_K, ϕ_K	The azimuthal and polar angles describing the orientation of the spin angular momentum vector of the MBH	Uniform $[10^{-3}, \pi]$
$\Phi_{\varphi,0}, \Phi_{\theta,0}, \Phi_{r,0}$	The phase of azimuthal, polar, and radial modes	Fix $[0]$

(c) Parameters space of GB dataset		
Parameter	Description	Parameter distribution
f	Frequency	log-Uniform $[-4, -2]$ Hz
\dot{f}	The derivative of f	Fix $[10^{-14}]$
A	Amplitude	Uniform $[10^{-23}, 10^{-21}]$
ι_0, ψ, ϕ_0	The inclination angle, polarization angle and initial phase	Uniform $[0, \pi]$
λ	Ecliptic longitude	Uniform $[0, 2\pi]$
β	Ecliptic latitude	Uniform $[0, \pi]$

2. EMRIs

EMRIs are a kind of black hole binary system with a mass ratio of $m/M \simeq 10^{-4} - 10^{-7}$ and massive black holes have a mass range of $M \simeq 10^5 - 10^7 M_\odot$. EMRIs waveforms are able to encapsulate the properties of space-time near a massive black hole. EMRIs are among the primary detection targets for the space-based GW detectors, possessing the potential to unveil new physical phenomena[44–46]. We employ `FastEMRIsWaveforms` (FEW) package[47] to generate EMRIs waveforms with a sampling rate of 5s. A random slice of 4,200 points is selected to form a waveform for training and inference. Training dataset with randomly sampled parameters is repeatedly regenerated to guarantee complete parameter space coverage. Before feeding the waveform into the model, we standardized it to help the model capture the information from EMRIs waveforms. The parameter space of the EMRIs dataset is shown in Table I(b). The complexity of the EMRIs waveform is visible in Figure 2(b). As the eccentricity increases, the complexity of the

waveform also increases, which is more obvious in the frequency domain.

3. Galactic binary

Within the Milky Way galaxy, a substantial population of binary white dwarf systems exists, posing foreground noise challenges for space-based gravitational wave detectors. We use the following GB model (Equation 1) to generate GB waveform[48]:

$$\begin{aligned}
 h_+^{\text{src}}(t) &= \mathcal{A}(1 + \cos^2 \iota) \cos \Phi(t), \\
 h_\times^{\text{src}}(t) &= 2\mathcal{A} \sin \iota \sin \Phi(t), \\
 \Phi(t) &= \phi_0 + 2\pi f_0 t + \pi \dot{f}_0 t^2 + \frac{\pi}{3} \ddot{f}_0 t^3, \\
 \ddot{f}_0 &= \frac{11}{3} \frac{\dot{f}_0^2}{f_0}.
 \end{aligned} \tag{1}$$

Similar to EMRIs, GB waveforms are generated with a duration of 1 year and a sampling rate of 1/15 Hz. A

slice of 4,200 points is randomly truncated for training and inference. The parameter space of the GB dataset is shown in Table I(c).

4. Detector response and TDI 2.0

After generating the waveform, we project it into the LISA detector[49]:

$$h_{I,II}(t) = \frac{\sqrt{3}}{2} h_+(t) F_{I,II}^+(\theta_S, \phi_S, \psi_S) + \frac{\sqrt{3}}{2} h_\times(t) F_{I,II}^\times(\theta_S, \phi_S, \psi_S), \quad (2)$$

where $F_{I,II}^+$ and $F_{I,II}^\times$ are the antenna pattern functions, ϕ_S is the polarisation angle, θ_S, ϕ_S are the polar and azimuthal sky location angles, respectively. Space-based gravitational wave detectors have unequal arm lengths, which result in significant laser frequency noise. To mitigate this issue, TDI techniques are commonly employed to suppress laser frequency noise[50, 51]. As a result, the detector response and the second-generation Michelson combinations (TDI 2.0) response of GW are calculated using `FastLISAresponse`[52] in this case. TDI 2.0 generates three channels X, Y, and Z. By combining X, Y, and Z, three independent channels A, E, and T are obtained,

$$\begin{aligned} A &= (Z - X)/\sqrt{2}, \\ E &= (X - 2Y + Z)/\sqrt{6}, \\ T &= (X + Y + Z)/\sqrt{3}. \end{aligned} \quad (3)$$

In contrast to the waveform template, the incorporation of response functions and TDI 2.0 combination introduces increased complexity to the waveform, especially in the high-frequency part. As depicted in Figure 2, MBHB waveforms exhibit significant differences at various parameter values. The increase in complexity presents more challenges in our work while also making our method more practical in future space-based GW research.

B. CBS-GPT Model

Transformer[53] is a class of deep learning models that has exhibited excellent performance in various tasks, such as natural language processing (NLP)[40–42] and computer vision[54]. We incorporate the masked self-attention mechanism and feed-forward neural network of transformer to build our CBS-GPT model.

Patching Firstly, each input waveform x^i is divided into non-overlapping patches, and we refer to each patch as a "token" here. The number of tokens depends on the length of each patch and the total length of the waveform. For all three types of signal sources, we have an input waveform with 4,200 sampling points, which is segmented into 1,050 tokens, and each token has a length of 4. Prior

to patching, the input waveform is preprocessed by Z-score normalization, which facilitates the model in capturing waveform information more effectively:

$$\text{Normal}(s) = \frac{s - \text{Mean}(s)}{\text{Std}(s)} \quad (4)$$

where s represents the input waveform, $\text{Mean}(\cdot)$ and $\text{Std}(\cdot)$ represent finding the mean and standard variance of the waveform respectively.

Hybrid Embedding Different from NLP applications, in our scenario, each token contains richer physical information, and can not be tokenized by common tokenizers as in NLP. Hence, the hybrid embedding module is utilized in our model. As Figure 1 shows, it includes a dense layer and positional embedding layer. The dense layer performs linear projection, which achieves dimension mapping and meanwhile preserves the entire information of the input sequence. The dense layer projects the token into a high-dimensional space of dimension $d_{model} = 1280$. The positional layer is also a linear layer with learnable parameters that encodes positional relationships between tokens, which is rather important in improving prediction accuracy[53].

Encoder block The encoder contains 36 blocks. Each block mainly consists of an attention module and a feed-forward neural network. As for the attention module, masked multi-head self-attention (MMHA) is adopted in our work, which enables information to be projected into matrices in different ways, thereby enhancing the expressive capacity of the model. The computation process of the attention module is as follows:

$$\text{head}_i(Q_i, K_i, V_i) = \text{softmax}\left(\frac{Q_i K_i^T \cdot \text{mask}}{\sqrt{d}}\right) V_i, \quad (5)$$

where $Q_i = W^Q x_i, K_i = W^K x_i, V_i = W^V x_i$ represent queries, keys and values of the i -th attention head respectively. Then, concatenate the outputs of all the heads and apply a linear transformation to obtain the final multi-head attention output:

$$\text{MMHA}(Q, K, V) = \text{Concat}(\text{head}_1, \dots, \text{head}_H) W^H, \quad (6)$$

$$H' = \text{LayerNorm}(\text{MMHA}(Q, K, V)) + x_i, \quad (7)$$

where x_i represents the hybrid embedding output or the output of the previous encoder block, and H' is the output of the attention module. In MMHA block, W^Q, W^K, W^V and W^H are learnable parameters.

The feed-forward network (**FFN**) that composed of two dense layers is connected to each attention module. In order to get better results, we employ the residual connection, which helps reduce the vanishing gradient problem.

$$\text{Inter}(H') = \text{GeLU}(H' W_1 + b_1) W_2 + b_2 \quad (8)$$

$$\text{FFN}(H') = \text{LayerNorm}(\text{Inter}(H')) + H' \quad (9)$$

Loss Function Mean Squared Error (MSE) loss is used to measure the difference between the predictions and the true values as Equation 10 illustrates.

$$\mathcal{L} = \mathbb{E}_{\mathbf{y}} \frac{1}{M} \sum_{i=1}^M \|\hat{\mathbf{y}}^{(i)} - \mathbf{y}^{(i)}\|_2^2. \quad (10)$$

Where $\mathbf{y}^{(i)}$ and $\hat{\mathbf{y}}^{(i)}$ represent prediction and true value of each token. M represents the total input sampling points which equals 4,200.

C. Training and Inference

CBS-GPT contains a total of 36 encoder blocks, with each block having 20 attention heads. The hidden size of each attention head is 64. And the hidden size of two dense layers of FFN is 5,120 and 1,280, respectively. During training, Adam[55] optimizer with $\beta_1 = 0.9$, $\beta_2 = 0.999$ is used, and the initial learning rate is $2e-4$. To make sure that the training dataset covers the entire parameter space, the training dataset is continuously updated, and the parameters of each waveform are randomly selected from the parameter space of the sources during training. After passing through the LISA response, each waveform is divided into three channels (A, E, and T). In this study, the E channel is selected to train the model. The model was trained on two NVIDIA V100 GPU for approximately 30 hours.

During inference, the initial input sequence contains 1,000 valid tokens and 50 masked tokens that are masked with zero, whose corresponding value in the mask matrix equals 1. In the first step, the 1,001-st token is predicted and replaces the previous 1,001-st token, and so forth, 50 successive tokens are predicted based on 1,000 valid input tokens.

III. RESULTS AND DISCUSSION

A. Overlap Result

During inference, for each signal source, 10,000 waveforms with random uniform parameter distribution are generated to test GP-GPT's performance. By providing the former part of each signal (4,000 sampling points), the following 200 sampling points are extrapolated through CBS-GPT. Overlap is defined to evaluate the extrapolation accuracy of the predicted waveform.

Overlap is calculated between the target waveform and predicted waveform generated by CBS-GPT as stated in Equation 11. The overlap \mathcal{O} ranges between $[0, 1]$, with values closer to 1 indicating that the predicted waveform is more similar to the target waveform.

$$\mathcal{O}(h_t, h_p) = \max_{t_c} \left(\hat{h}_t | \hat{h}_p [t_c] \right)^{1/2}, \quad (11)$$

with

$$(h|s) = 2 \int_{f_{\min}}^{f_{\max}} \frac{\tilde{h}^*(f) \tilde{s}(f) + \tilde{h}(f) \tilde{s}^*(f)}{S_n(f)} df, \quad (12)$$

$$\hat{h} = \frac{h}{\sqrt{(h|h)}}$$

where t_c represents time-shifted and we set $S_n(f) = 1$. Overall, in the context of extrapolation tasks targeting MBHB, GB, and EMRIs signals, CBS-GPT has demonstrated remarkable efficacy, with over 50% of the overlaps exceeding 0.99. These results illustrate CBS-GPT's capability to learn from instrumentally responsive gravitational waveforms. Figure 3 demonstrates the prediction performance of each waveform under varying parameter conditions. This demonstrates that the CBS-GPT model can learn waveform characteristics with a wide variety of parameters.

1. Results of MBHB

During inference, as described in Section II C, a consistent input-to-prediction length ratio of 20:1 is applied. The distribution of overlap and examples of predicted waveforms are shown in Figure 3(a) and Figure 4(a), with mean and median overlap of 0.981 and 0.992, respectively. In particular, because of the short merge-ringdown phase, a smaller time range is shown on the left sub-figure in Figure 4(a). The overlap results reveal that CBS-GPT can forecast the waveform of the merge-ringdown phase based on the inspiral phase characteristics. CBS-GPT exhibits optimal inference performance when considering a total mass of approximately $10^{6.5} M_{\odot}$ as shown in Figure 3(a). Our observations reveal a notable pattern: CBS-GPT is similar to the gravitational wave detector that has its sensitive frequency band, as the MBHB waveform frequency is directly linked to the total mass of MBHB. This phenomenon has also been observed in other signal sources.

In particular, the CBS-GPT model is sensitive to total mass, mass ratio, and spin parameters. Here we use the effective spin parameter χ_{eff} to represent the spin parameter [56]:

$$\chi_{\text{eff}} = \frac{S_1^z}{1+q} + \frac{qS_2^z}{1+q}. \quad (13)$$

The overlap is higher in low total mass and high effective spin χ_{eff} area as shown in Figure 3(a). As the total mass decreases, the frequency of its waveform gradually increases. Since the TDI 2.0 transfer functions in the high-frequency part is more complex[57, 58], the waveform is also more complex. Consequently, the model's performance experiences a slight decrease. Nevertheless, as depicted in the left panel of Figure 4(a), CBS-GPT demonstrates the ability to learn the predominant features of the waveform, even in the presence of a complex

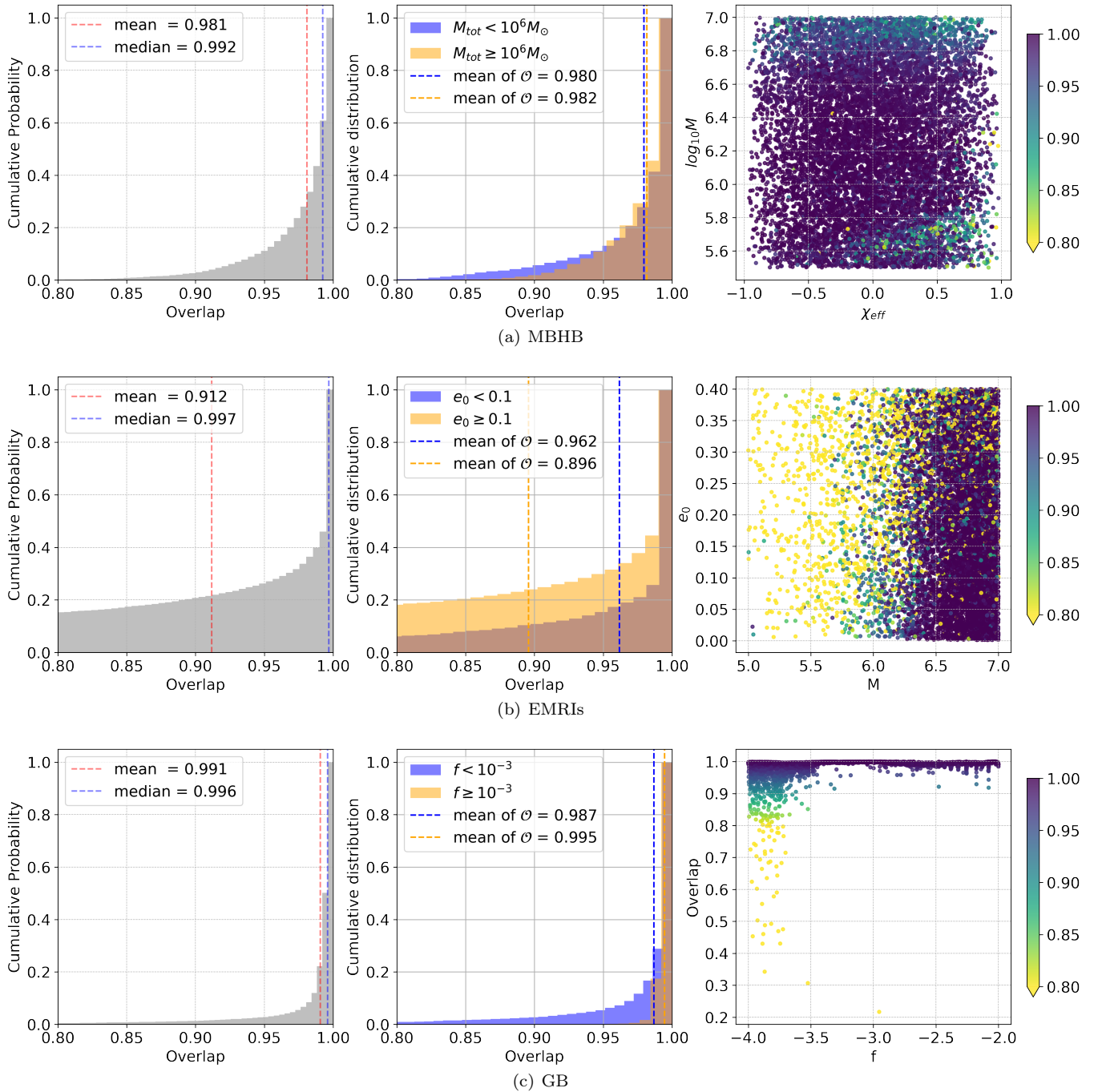


Figure 3. **The overlap distributions of MBHB, EMRIs, and GB are shown in the left panel. The parameters that have a greater impact on overlap are displayed in the middle and the right panels. MBHB, EMRIs, and GB have a mean overlap of 0.981, 0.912, and 0.991, respectively. (a) For MBHB waveforms, the biggest impact on the prediction results is M_{tot} and spin parameters χ_{eff} . The middle sub-figure showcases differences in overlap distribution associated with M_{tot} , and the right sub-figure portrays the overlap heat map of M_{tot} and χ_{eff} . (b) For EMRIs waveforms, e_0 and M have the greatest impact on overlap. As e_0 increases, the EMRIs waveform becomes increasingly complex. The middle sub-figure showcases differences in overlap distribution associated with e_0 , and the right sub-figure portrays the overlap heat map of e_0 and M . (c) For GB waveforms, the parameter with the greatest impact is the frequency parameter. The middle sub-figure showcases differences in overlap distribution associated with f , and the right sub-figure portrays the overlap heat map of f and overlap.**

waveform. While at lower frequencies (or higher total mass), the accumulation period of the input waveform is constrained. Comparing low and high-mass situations to those involving intermediate masses, the performance of mid-frequency band prediction is the best. Moreover, even in these less ideal circumstances, CBS-GPT still can successfully recover a significant portion of the signals.

2. Results of Continuous Waveform: EMRIs and GB

Similarly, CBS-GPT tests are performed on 10,000 EMRIs and GB waveforms with a 20:1 extrapolation rate. Overlap distribution of the EMRIs and GB is shown in Figure 3(b) and Figure 3(c), respectively. Regarding GB, its mean and median overlap both exceed 0.99. And mean and median overlap of EMRIs are equal to 0.912 and 0.997, respectively. While the mean overlap of EMRIs is slightly lower, its median overlap aligns with that observed in the MBHB and GB waveforms. Examples of predicted EMRIs and GB waveform are shown in Figure 4(b) and Figure 4(c).

Specifically, the overlap distribution of EMRIs significantly influenced by the mass parameters and eccentricity parameters. As depicted in Figure 3(b), when e_0 is less than 0.1, the majority of overlaps remain below 0.9. As the eccentricity increases, the waveform features become more complex in waveform amplitude. Therefore, when the eccentricity is higher, the corresponding overlap tends to decrease.

In contrast to MBHB and EMRIs signals, the GB signal presents a comparatively straightforward, single-frequency waveform. In the GB dataset, the frequency parameter has the greatest impact on the waveform. When the frequency is $> 10^{-3.5}$ Hz, the overlap is basically higher than 0.9. The overlap analysis for GB signals demonstrates the model’s frequency sensitivity, with a distinct preference for learning the characteristics associated with intermediate frequency signals. Meanwhile, as the extrapolation length increases, the prediction accuracy for the three sources decreases.

B. Interpretability

From a probabilistic perspective, CBS-GPT’s prediction of the waveform can be expressed by the conditional probability of predicting the next token as x_{i+1} by given the previous i tokens[41]:

$$L(x_{i+1}) = \sum_{k=1}^{i-1} \log P(x_i | x_{i-k}, \dots, x_1; \Theta), \quad (14)$$

where Θ represents the model parameters. The probability can be represented by the attention mechanism, which can be effectively visualized by an attention map. The attention map allows us to visualize the reasoning process

and attention mechanism when predicting waveform, making it easier to get knowledge to interpret gravitational wave data. Here, the inference process is visualized using the attention map:

$$A = \frac{1}{H} \sum_{i=1}^H \text{softmax}\left(\frac{Q_i K_i^T \cdot \text{mask}}{\sqrt{d}}\right), \quad (15)$$

where H represents all attention heads of the last encoder block. In Figure 5, the vertical axis represents the model input waveform, and the horizontal axis represents the predicted waveform.

When predicting continuous gravitational waveforms (EMRIs and GB), CBS-GPT tends to pay attention to the input points of the same phase, and the periodicity is shown in each row and column of the attention map (Figure 5(g) - 5(f)). The attention map exhibits a grid-like pattern that is closely related to the phase of the waveform, with the scale of the grid expanding as the frequency decreases. Hence, we perform a correlation calculation between the waveform and the hidden parameters, with detailed information available in Appendix A. In our sample, the correlation coefficient for continuous waveforms exceeds 0.8. This demonstrates that the model can accurately match the waveform’s frequency and phase information. This mode assists CBS-GPT in successfully extrapolating input data, demonstrating its capacity to learn information across various scales.

During the prediction of the merge-ringdown phase of MBHB waveforms, attention primarily focuses on near-diagonal elements as showcased in Figure 5(a) - 5(c). In contrast to the continuous gravitational wave signals, the emphasis is more centralized around the information proximate to the merger phase. The amplitude reaches zero after the merge-ringdown, and the main focus of the attention mechanism lies on the merging stage and the stage after the merge, with relatively less attention directed towards information in the inspiral phase. The focus of the attention map also changes under different total masses, which demonstrates that CBS-GPT predicts waveforms by matching waveform phases and frequency. Moreover, as Figure 4 demonstrates that CBS-GPT accurately estimates the main frequency, the attention map also effectively captures the phase information of the waveform.

IV. CONCLUSION

In this paper, we introduce the CBS-GPT model, which consists of hybrid embedding and encoder blocks. The CBS-GPT is applied to the prediction of GW waveform after the response of the space-based gravitational wave detector and TDI 2.0 combination. Three models are trained separately for MBHB, EMRIs, and GB wave sources to predict the next 200-point waveform by feeding the previous 4,000-point waveform. In the case of complex instrument response, wide parameter range, and large

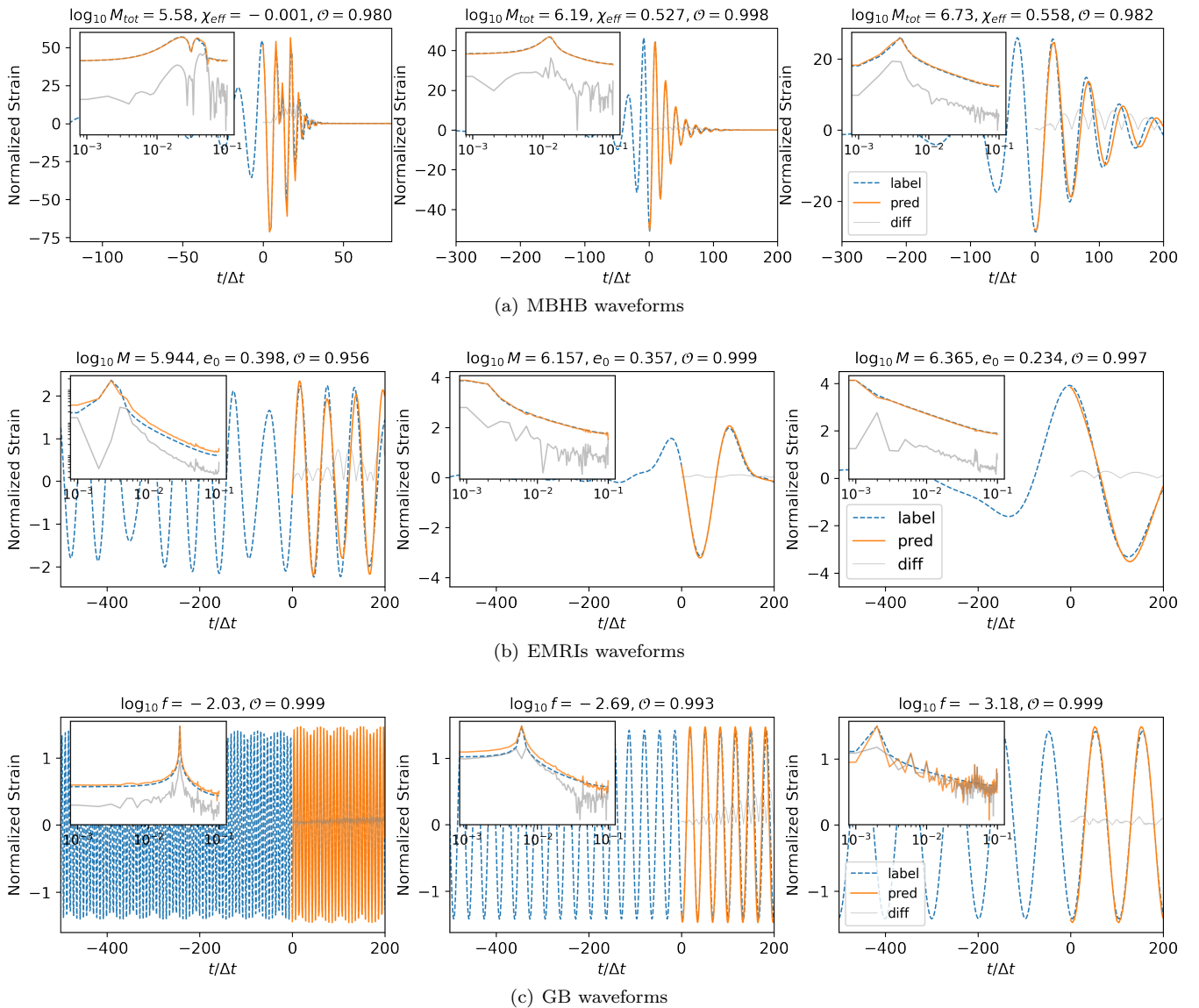


Figure 4. **CBS-GPT prediction results of MBHB, EMRIs, and GB.** We set the predicted starting point at time zero. To clarify, the blue line represents the conjunction of the last part of the input waveform and target label, the orange line is the predicted waveform, and the gray line is the difference between the predicted and target waveform. The subfigure on the upper-left represents the corresponding spectrum and difference in the frequency domain.

frequency band span, the average overlaps between the predicted waveform and the target waveform of MBHB, EMRIs, and GB reach 0.981, 0.912, and 0.991, respectively. Intermediate-frequency waveforms exhibit superior prediction performance compared to both high-frequency and low-frequency counterparts.

At the same time, the visualization of the attention map illustrates that CBS-GPT adjusts the attention map based on the varying frequencies of the waveform. We discovered that the correlation coefficient between the hidden parameters of the CBS-GPT model and the waveforms is relatively high, indicating that the model can match the waveform’s phase information extremely well. This allows our model to accurately match phase and fre-

quency information. Our results show that CBS-GPT has the ability to comprehend detailed waveform properties, make predictions based on the input waveform data, and exhibit remarkable learning performance over waveforms of varied frequencies. We are confident that large models can be further used in gravitational wave data processing in the future. For instance, the powerful learning capabilities of CBS-GPT hold the potential for future applications in tasks such as the gap completion of data from space-based GW detectors, GW signal detection, and signal noise reduction.

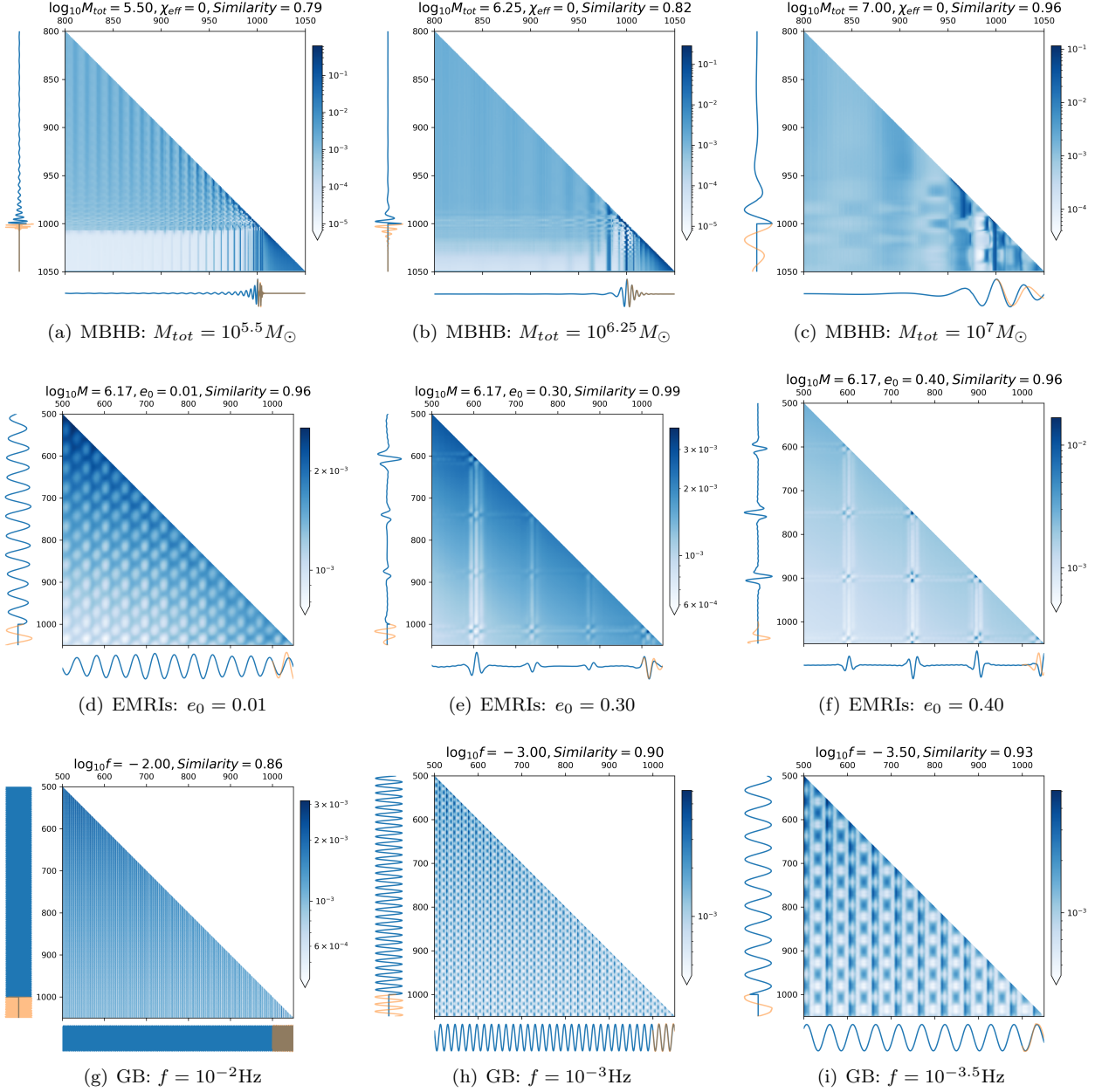


Figure 5. **Attention maps of the last encoder layer.** For clear presentation, only part of the attention map is displayed. The blue lines on the left and bottom panels represent the input waveforms, whose 1,001-st to 1,050-th tokens are padded with zero-value during inference, and the orange line represents the waveform predicted by CBS-GPT. The term **Similarity** in the title of each figure denotes the correlation coefficient between the waveform and the hidden parameters, which is significantly high.

ACKNOWLEDGMENTS

This research was supported by the Peng Cheng Laboratory and Peng Cheng Cloud-Brain. This work was also supported in part by the National Key Research and Development Program of China Grant No. 2021YFC2203001 and in part by the NSFC (No. 11920101003 and No. 12021003). Z.C. was supported by the “Interdisciplinary Research Funds of Beijing Normal University” and CAS

Project for Young Scientists in Basic Research YSBR-006.

Appendix A: Correlation coefficient between waveform and hidden parameters

We introduce the correlation coefficient between the waveform and hidden parameters to assess the level of correlation and demonstrate that the attention map can

capture the phase information of the waveform. Firstly, we compute the mean value of each token of the patched input to get the sequence M . Subsequently, the outer product of M is computed, resulting in the auto-correlation matrix. As the attention map is processed by masking and normalized by the softmax function, we do a similar adjustment to the auto-correlation matrix as Equation

A1 shows.

$$\begin{aligned} R_{\text{mask}} &= \text{Mask}(M \otimes M - \min(M \otimes M)) \\ R_{\text{Norm}} &= \text{RowNorm}(R_{\text{mask}}), \end{aligned} \quad (\text{A1})$$

where $\text{RowNorm}(\cdot)$ denotes the normalization of each row of the matrix. To assess the correlation between the two matrices, we calculate the Pearson correlation coefficient between the flattened attention map and flattened R_{Norm} (Equation A2):

$$\rho_{A, R_{\text{Norm}}} = \rho\{\text{Flatten}(A), \text{Flatten}(R_{\text{Norm}})\} = \frac{n \sum_1^n A_{F_i} R_{F_i} - \sum_1^n A_{F_i} \sum_1^n R_{F_i}}{\sqrt{n \sum_1^n A_{F_i}^2 - (\sum_1^n A_{F_i})^2} \sqrt{n \sum_1^n R_{F_i}^2 - (\sum_1^n R_{F_i})^2}} \quad (\text{A2})$$

where $\text{Flatten}(\cdot)$ denotes flattening the matrix into one dimension, and n represents the length after flattening.

Finally, $\rho_{A, R_{\text{Norm}}}$ is defined as the correlation coefficient between waveform and hidden parameters.

-
- [1] B. P. Abbott, R. Abbott, T. D. Abbott, M. R. Abernathy, F. Acernese, K. Ackley, C. Adams, T. Adams, P. Addesso, R. X. Adhikari, et al., *Physical Review Letters* **116**, 061102 (2016).
- [2] B. P. Abbott, R. Abbott, T. D. Abbott, M. R. Abernathy, F. Acernese, K. Ackley, C. Adams, T. Adams, P. Addesso, R. X. Adhikari, et al., *Physical Review D* **93**, 122003 (2016).
- [3] B. F. Schutz, *Nature* **323**, 310 (1986).
- [4] B. S. Sathyaprakash and B. F. Schutz, *Living Reviews in Relativity* **12**, 2 (2009).
- [5] A. Klein, E. Barausse, A. Sesana, A. Petiteau, E. Berti, S. Babak, J. Gair, S. Aoudia, I. Hinder, F. Ohme, et al., *Physical Review D* **93**, 024003 (2016), [arxiv:1511.05581 \[astro-ph, physics:gr-qc\]](#).
- [6] N. Tamanini, C. Caprini, E. Barausse, A. Sesana, A. Klein, and A. Petiteau, *Journal of Cosmology and Astroparticle Physics* **2016**, 002 (2016), [arxiv:1601.07112 \[astro-ph, physics:gr-qc\]](#).
- [7] N. Bartolo, C. Caprini, V. Domcke, D. G. Figueroa, J. Garcia-Bellido, M. C. Guzzetti, M. Liguori, S. Matarrese, M. Peloso, A. Petiteau, et al., *Journal of Cosmology and Astroparticle Physics* **2016**, 026 (2016), [arxiv:1610.06481 \[astro-ph, physics:gr-qc, physics:hep-ph\]](#).
- [8] C. Caprini, M. Hindmarsh, S. Huber, T. Konstandin, J. Kozaczuk, G. Nardini, J. M. No, A. Petiteau, P. Schwaller, G. Servant, et al., *Journal of Cosmology and Astroparticle Physics* **2016**, 001 (2016), [arxiv:1512.06239 \[astro-ph, physics:gr-qc, physics:hep-ph\]](#).
- [9] S. Babak, J. Gair, A. Sesana, E. Barausse, C. F. Sopuerta, C. P. L. Berry, E. Berti, P. Amaro-Seoane, A. Petiteau, and A. Klein, *Physical Review D* **95**, 103012 (2017), [arxiv:1703.09722 \[astro-ph, physics:gr-qc\]](#).
- [10] K. G. Arun, E. Belgacem, R. Benkel, L. Bernard, E. Berti, G. Bertone, M. Besancon, D. Blas, C. G. Böhrer, R. Brito, et al., *Living Reviews in Relativity* **25**, 4 (2022), [arxiv:2205.01597 \[gr-qc\]](#).
- [11] T. L. S. Collaboration, the Virgo Collaboration, the KAGRA Collaboration, R. Abbott, T. D. Abbott, F. Acernese, K. Ackley, C. Adams, N. Adhikari, R. X. Adhikari, et al., “GWTC-3: Compact Binary Coalescences Observed by LIGO and Virgo During the Second Part of the Third Observing Run,” (2021), [arxiv:2111.03606 \[astro-ph, physics:gr-qc\]](#).
- [12] G. Agazie, A. Anumarlapudi, A. M. Archibald, Z. Arzoumanian, P. T. Baker, B. Bécsy, L. Blecha, A. Brazier, P. R. Brook, S. Burke-Spolaor, et al., *The Astrophysical Journal Letters* **951**, L8 (2023).
- [13] H. Xu, S. Chen, Y. Guo, J. Jiang, B. Wang, J. Xu, Z. Xue, R. N. Caballero, J. Yuan, Y. Xu, et al., *Research in Astronomy and Astrophysics* **23**, 075024 (2023), [arxiv:2306.16216 \[astro-ph, physics:gr-qc\]](#).
- [14] EPTA Collaboration and InPTA Collaboration:, J. Antoniadis, P. Arumugam, S. Arumugam, S. Babak, M. Bagchi, A.-S. Bak Nielsen, C. G. Bassa, A. Bathula, A. Berthereau, et al., *Astronomy & Astrophysics* **678**, A50 (2023).
- [15] D. J. Reardon, A. Zic, R. M. Shannon, G. B. Hobbs, M. Bailes, V. Di Marco, A. Kapur, A. F. Rogers, E. Thrane, J. Askew, et al., *The Astrophysical Journal Letters* **951**, L6 (2023).
- [16] M. Bailes, B. K. Berger, P. R. Brady, M. Branchesi, K. Danzmann, M. Evans, K. Holley-Bockelmann, B. R. Iyer, T. Kajita, S. Katsanevas, et al., *Nature Reviews Physics* **3**, 344 (2021).
- [17] P. Amaro-Seoane, H. Audley, S. Babak, J. Baker, E. Barausse, P. Bender, E. Berti, P. Binetruy, M. Born, D. Borotoluzzi, et al., “Laser Interferometer Space Antenna,” (2017), [arxiv:1702.00786 \[astro-ph\]](#).
- [18] W.-R. Hu and Y.-L. Wu, *National Science Review* **4**, 685 (2017).
- [19] Z. Ren, T. Zhao, Z. Cao, Z.-K. Guo, W.-B. Han, H.-B. Jin, and Y.-L. Wu, *Frontiers of Physics* **18**, 64302 (2023).
- [20] J. Luo, L.-S. Chen, H.-Z. Duan, Y.-G. Gong, S. Hu, J. Ji, Q. Liu, J. Mei, V. Milyukov, M. Sazhin, et al.,

- Classical and Quantum Gravity **33**, 035010 (2016), [arxiv:1512.02076 \[astro-ph, physics:gr-qc\]](#).
- [21] F. Matichard, B. Lantz, R. Mittleman, K. Mason, J. Kissel, B. Abbott, S. Biscans, J. McIver, R. Abbott, S. Abbott, et al., *Classical and Quantum Gravity* **32**, 185003 (2015).
- [22] H. Wang, S. Wu, Z. Cao, X. Liu, and J.-Y. Zhu, *Physical Review D* **101**, 104003 (2020).
- [23] D. George and E. Huerta, *Physics Letters B* **778**, 64 (2018).
- [24] D. George and E. A. Huerta, *Physical Review D* **97**, 044039 (2018).
- [25] H. Gabbard, M. Williams, F. Hayes, and C. Messenger, *Physical Review Letters* **120**, 141103 (2018).
- [26] C. Badger, K. Martinovic, A. Torres-Forné, M. Sakellariadou, and J. A. Font, *Physical Review Letters* **130**, 091401 (2023).
- [27] X.-T. Zhang, C. Messenger, N. Korsakova, M. L. Chan, Y.-M. Hu, and J.-d. Zhang, *Physical Review D* **105**, 123027 (2022), [arxiv:2202.07158 \[astro-ph, physics:gr-qc\]](#).
- [28] M. Dax, S. R. Green, J. Gair, J. H. Macke, A. Buonanno, and B. Schölkopf, *Physical Review Letters* **127**, 241103 (2021).
- [29] H. Gabbard, C. Messenger, I. S. Heng, F. Tonolini, and R. Murray-Smith, *Nature Physics* **18**, 112 (2022).
- [30] H. Wang, Z. Cao, Y. Zhou, Z.-K. Guo, and Z. Ren, *Big Data Mining and Analytics* **5**, 53 (2022).
- [31] T. Zhao, R. Lyu, H. Wang, Z. Cao, and Z. Ren, *Communications Physics* **6**, 212 (2023).
- [32] R. Ormiston, T. Nguyen, M. Coughlin, R. X. Adhikari, and E. Katsavounidis, *Physical Review Research* **2**, 033066 (2020).
- [33] W. Wei and E. Huerta, *Physics Letters B* **800**, 135081 (2020).
- [34] R. E. Colgan, K. R. Corley, Y. Lau, I. Bartos, J. N. Wright, Z. Márka, and S. Márka, *Physical Review D* **101**, 102003 (2020).
- [35] Z. Ren, H. Wang, Y. Zhou, Z.-K. Guo, and Z. Cao, “Intelligent noise suppression for gravitational wave observational data,” (2022), [arxiv:2212.14283 \[astro-ph, physics:gr-qc\]](#).
- [36] J. Lee, S. H. Oh, K. Kim, G. Cho, J. J. Oh, E. J. Son, and H. M. Lee, *Physical Review D* **103**, 123023 (2021), [arxiv:2101.05685 \[astro-ph, physics:gr-qc\]](#).
- [37] A. Khan, E. A. Huerta, and H. Zheng, *Physical Review D* **105**, 024024 (2022), [arxiv:2110.06968 \[astro-ph, physics:gr-qc\]](#).
- [38] A. J. K. Chua, C. R. Galley, and M. Vallisneri, *Physical Review Letters* **122**, 211101 (2019), [arxiv:1811.05491 \[astro-ph, physics:gr-qc, stat\]](#).
- [39] J. Devlin, M. Chang, K. Lee, and K. Toutanova, “BERT: pre-training of deep bidirectional transformers for language understanding,” (2019).
- [40] A. Radford and K. Narasimhan, (2018).
- [41] A. Radford, J. Wu, R. Child, D. Luan, D. Amodei, and I. Sutskever, (2019).
- [42] T. B. Brown, B. Mann, N. Ryder, M. Subbiah, J. Kaplan, P. Dhariwal, A. Neelakantan, P. Shyam, G. Sastry, A. Askell, et al., *Advances in Neural Information Processing Systems 33: Annual Conference on Neural Information Processing Systems 2020, NeurIPS 2020, December 6-12, 2020, virtual*, (2020).
- [43] A. Bohé, L. Shao, A. Taracchini, A. Buonanno, S. Babak, I. W. Harry, I. Hinder, S. Ossokine, M. Pürrer, V. Raymond, et al., *Physical Review D* **95**, 044028 (2017), [arxiv:1611.03703 \[gr-qc\]](#).
- [44] S. Babak, J. Gair, A. Sesana, E. Barausse, C. F. Sopuerta, C. P. L. Berry, E. Berti, P. Amaro-Seoane, A. Petiteau, and A. Klein, *Physical Review D* **95**, 103012 (2017).
- [45] A. Maselli, N. Franchini, L. Gualtieri, T. P. Sotiriou, S. Barsanti, and P. Pani, *Nature Astronomy* **6**, 464 (2022).
- [46] P. Amaro-Seoane, J. Andrews, M. Arca Sedda, A. Askar, Q. Baghi, R. Balasov, I. Bartos, S. S. Bavera, J. Bellovary, C. P. L. Berry, et al., *Living Reviews in Relativity* **26**, 2 (2023).
- [47] M. L. Katz, A. J. K. Chua, L. Speri, N. Warburton, and S. A. Hughes, *Physical Review D* **104**, 064047 (2021).
- [48] X.-H. Zhang, S.-D. Zhao, S. D. Mohanty, and Y.-X. Liu, *Physical Review D* **106**, 102004 (2022), [arxiv:2206.12083 \[gr-qc\]](#).
- [49] T. Robson, N. Cornish, and C. Liu, *Classical and Quantum Gravity* **36**, 105011 (2019), [arxiv:1803.01944 \[astro-ph, physics:gr-qc\]](#).
- [50] M. Tinto, F. B. Estabrook, and J. W. Armstrong, *Physical Review D* **69**, 082001 (2004).
- [51] M. Tinto and S. V. Dhurandhar, *Living Reviews in Relativity* **17**, 6 (2014).
- [52] M. L. Katz, J.-B. Bayle, A. J. K. Chua, and M. Vallisneri, *Physical Review D* **106**, 103001 (2022), [arxiv:2204.06633 \[astro-ph, physics:gr-qc\]](#).
- [53] A. Vaswani, N. Shazeer, N. Parmar, J. Uszkoreit, L. Jones, A. N. Gomez, L. Kaiser, and I. Polosukhin, “Attention is all you need,” (2017).
- [54] Z. Liu, Y. Lin, Y. Cao, H. Hu, Y. Wei, Z. Zhang, S. Lin, and B. Guo, “Swin transformer: Hierarchical vision transformer using shifted windows,” (2021).
- [55] D. P. Kingma and J. Ba, “Adam: A method for stochastic optimization,” (2017), [arxiv:1412.6980 \[cs\]](#).
- [56] L. Barack, V. Cardoso, S. Nissanke, T. P. Sotiriou, A. Askar, C. Belczynski, G. Bertone, E. Bon, D. Blas, R. Brito, et al., *Classical and Quantum Gravity* **36**, 143001 (2019).
- [57] S. L. Larson, W. A. Hiscock, and R. W. Hellings, *Physical Review D* **62**, 062001 (2000), [arxiv:gr-qc/9909080](#).
- [58] S. Babak, M. Hewitson, and A. Petiteau, “LISA Sensitivity and SNR Calculations,” (2021), [arxiv:2108.01167 \[astro-ph, physics:gr-qc\]](#).